www.sciencemag.org/cgi/content/full/science.1260279/DC1

Supplementary Materials for

Ongoing drought-induced uplift in the western United States

Adrian Antal Borsa,* Duncan Carr Agnew, Daniel R. Cayan

*Corresponding author. E-mail: aborsa@ucsd.edu

Published 21 August 2014 on *Science* Express
DOI: 10.1126/science.1260279

This PDF file includes:

Materials and Methods

Selection and Processing of GPS displacement data

Most of the GPS stations analyzed are part of the NSF's Earthscope Plate Boundary Observatory, which was designed to study crustal deformation along the boundary between the Pacific and North American tectonic plates in the western USA (WUSA). We used Level 2 daily position data archived by the NSF's GAGE Facility at UNAVCO, specifically the GPS time series file nmt.final_nam08.pos.tar.gz produced by the New Mexico Tech analysis center and available at ftp://data-out.unavco.org/pub/products/position/ (last accessed May 10, 2014). We did not use the combined PBO time series because it appears to be affected by a network-wide vertical shift in GPS week 1717 (December 2011) that appears in the Central Washington University analysis center's time series but not New Mexico Tech's.

We began by processing data from 874 stations between longitude 109W and the Pacific coast, using only those whose data (1) span the period 2010-2014, (2) are at least 75% complete, and (3) have no gap longer than 91 days. We detrended each time series to remove secular tectonic motion and removed seasonal displacements using the STL (Seasonal-Trend-Loess) procedure, smoothing the result by loess filtering with an L1 misfit criterion (Fig. S1). We used a smoothing parameter of 30 for the annual adjustment and smoothed over 72 days with the L1 loess smoother.

Before inverting for load, we removed all 27 stations located within a convex hull that bounds California's Central Valley (because of the widespread pumping occurring there) and all 14 stations in the vicinity of the actively-deforming Long Valley caldera. We also removed 42 stations whose maximum vertical uplift does not occur during the summer and fall (mid-July through the end of October). This procedure has been used by other investigators to identify stations located above actively-pumped aquifers, since heavy pumping during the summer causes subsidence rather than to the expected uplift due to seasonal drying. From the remaining stations, we removed 12 outliers whose vertical displacement in March 2014 relative to the median displacement of the entire network was more than 3.5 times the interquartile range, leaving 771 stations as the basis of our analysis.

We also analyzed the ratio of vertical to horizontal displacements to assess whether tectonic or volcanic processes might be impacting our results. The only areas where the magnitude of horizontal displacements in March 2014 consistently exceeded that of vertical displacements were Yellowstone (which is an active caldera) and the Salton Trough (which is still undergoing post-seismic displacement from the 2010 El Mayor-Cucapah earthquake), both reflecting local processes with local impacts.

Inversion for Mass Loss

For each GPS site, we calculated the vertical displacement from a unit load at each element of a 0.5-degree grid spanning the WUSA. For this calculation we used the SPOTL program (see next section), which uses the Green functions for the response of an elastic Earth to surface

loads. These responses were used to construct the Jacobian matrix for a Gauss-Newton inversion that minimized the root mean square (rms) difference between predicted displacements and their average observed values in March 2014. We stabilized the inversion by applying a minimum-curvature (smoothness) constraint to the gridded loads, and varied the weighting of this constraint relative to misfit to recover loading models of varying smoothness (Fig. S5, S6). For our analysis we chose a model that balanced misfit and smoothness (Fig. 3).

Fig. S6 shows that the total deficit is insensitive to the imposed smoothness in the inversion. The model we choose has a total deficit of 238 Gt, which is the minimum amount; a plausible range of the tradeoff suggests an upper limit no more than a few percent higher. This is in keeping with the result of doing an inversion from the uplift from a uniform layer, which recovers a uniform layer and the layer thickness to within a few percent. In addition there will be uncertainty arising from the error in the GPS verticals, which we believe is no more than 10% of the signal.

Stress change calculations

To compute the stress change from the load model (and displacements for the inversion), we used the SPOTL tidal loading package (http://igppweb.ucsd.edu/~agnew/Spotl/spotlmain.html, last accessed July 25, 2014). We found the surface strain caused by the load estimate in Fig. 3 and converted this to maximum Coulomb stress change *(27)*. Stress rates were those given directly on the fault from a dislocation model, using estimated rates and locking depths.

Calculation of precipitation and stream discharge values

We obtained daily precipitation (rain plus snow) data from NOAA's Global Historical Climatology Network (version: GHCN Daily 3.12-upd-2014032905, http://www.ncdc.noaa.gov/oa/climate/ghcn-daily/, last accessed on March 30, 2014) and extracted data for 7078 stations within the western conterminous USA west of longitude 107W. We first smoothed the precipitation time series for each station by convolving each data point with a trailing 365-day boxcar window, excluding missing data points from the convolution, and calculated the median value for the period 2003-2014. We then calculated the deviation of each smoothed time series from the series median as a percentage, which gives values ranging from 0% in a precipitation-free year to over 200% for particularly wet years. Fig.4 shows the % deviation of annual precipitation ending on March 1 of 2011, 2012, 2013, and 2014.

In the case of stream discharge, we used data from the USGS National Streamflow Information Program (NSIP; http://water.usgs.gov/nsip/, last accessed March 25, 2014) and processed it identically to the precipitation data. The result is a set of plots (Fig. S8) of 2950 stations, analogous to the precipitation plots in Fig. 4.

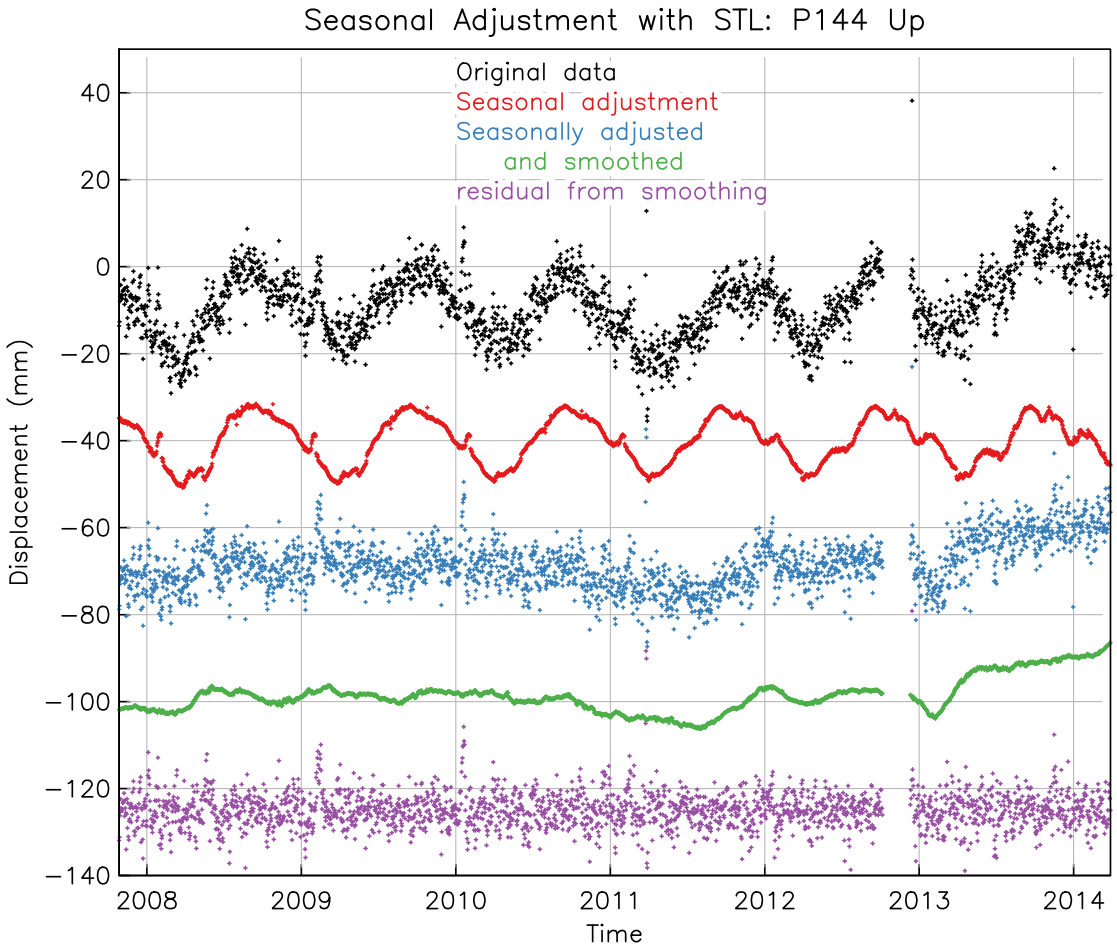

Fig. S1.

Example of how GPS time-series were processed. The plotted daily values show the decomposition into seasonal (red), smoothed non-seasonal (green) and residual (purple), for station P144, in the Sierra Nevada (NNE of Nevada City at 39.47N, 120.89W, 1440 m elevation). The smoothed non-seasonal time series for all stations are plotted in Fig. 1, in which the higher variability before 2007 reflects the smaller number of stations and the concentration of the network in southern California, which allowed local effects to dominate the WUSA median value.

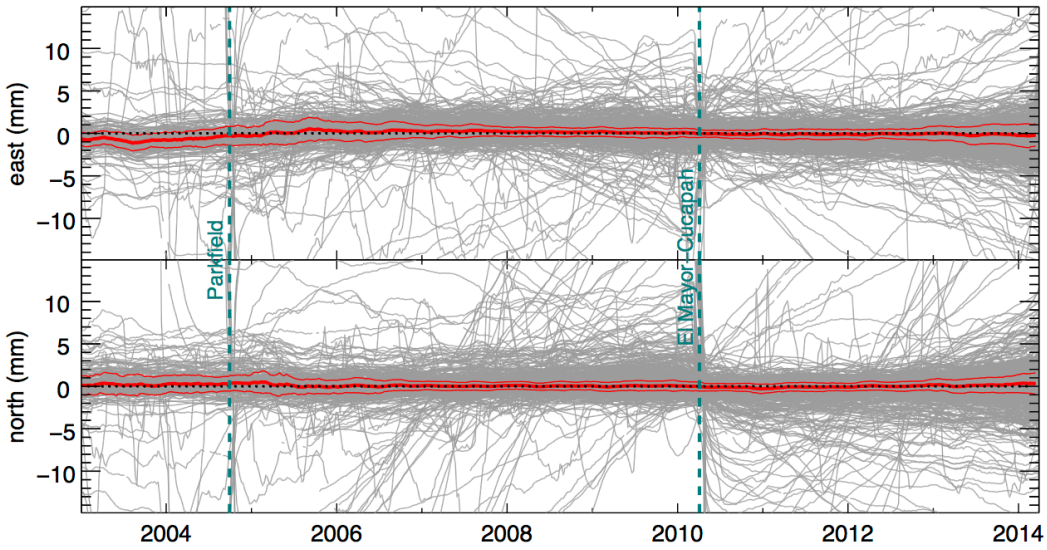

Fig. S2

Smoothed non-seasonal horizontal displacements plotted on the same scale as the vertical displacements in Fig. 1. The thick red line shows the median value of all data for each day, the light red lines shows the corresponding standard deviation computed from the interquartile range, and the dotted aqua lines show the times of the 2004 Parkfield and 2010 El Mayor/Cucapah earthquakes, which were the only significant earthquakes in the western USA during this period. The median horizontal value remains within one standard deviation of zero from 2006~2014, in contrast to the median vertical displacement in Fig. 1, which rises sharply in 2013.

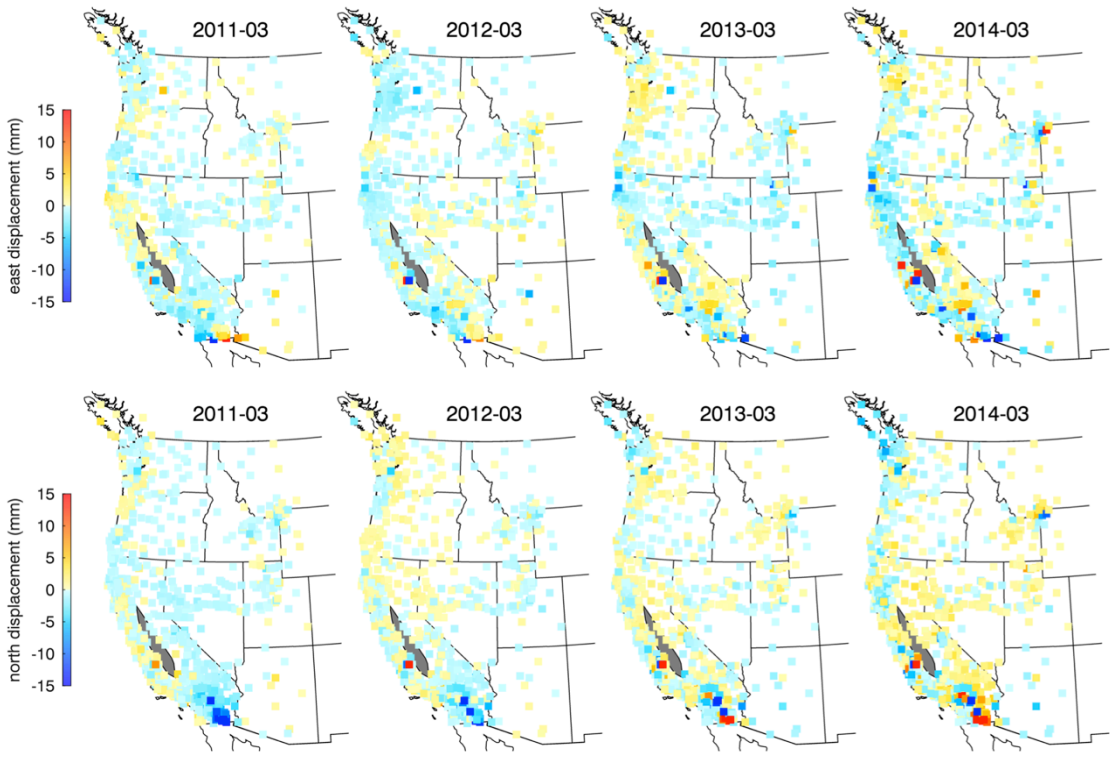

Fig. S3

Maps of East (top row) and North (bottom row) displacements corresponding to the vertical displacements in Fig. 2. Ongoing post-seismic deformation from the M_w7.2 2010 El Mayor/Cucapah earthquake is apparent on the California-Mexico border over the 2011~2014 period, as is a smaller area of deformation from the M_w6.0 2004 Parkfield earthquake. There are correlated areas of horizontal displacements apparent in the plots, but their magnitude is no more than a few cm and the median displacement over the entire region is zero for all epochs (see Fig. S2 and S4b).

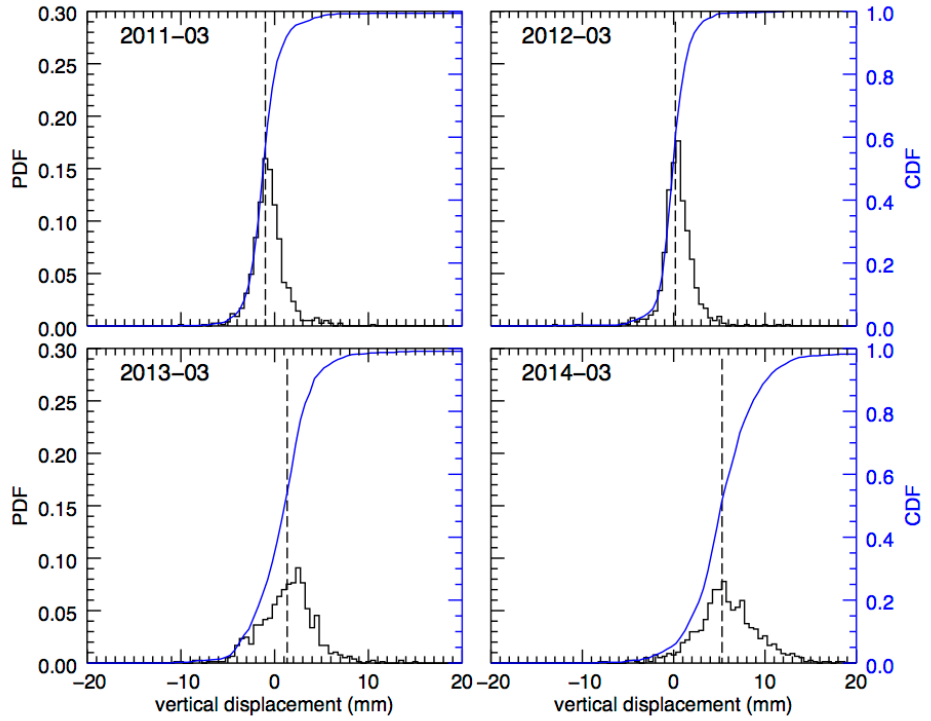

Fig. S4a

Histogram of all vertical displacements in Fig. 2, for each epoch shown. The blue line shows the cumulative distribution function, and the dashed line the median (indistinguishable from the mean in these cases). The WUSA uplift that begins as a small (1 mm) increase in the median vertical displacement in 2013 increases to a +5 mm displacement by March 2014.

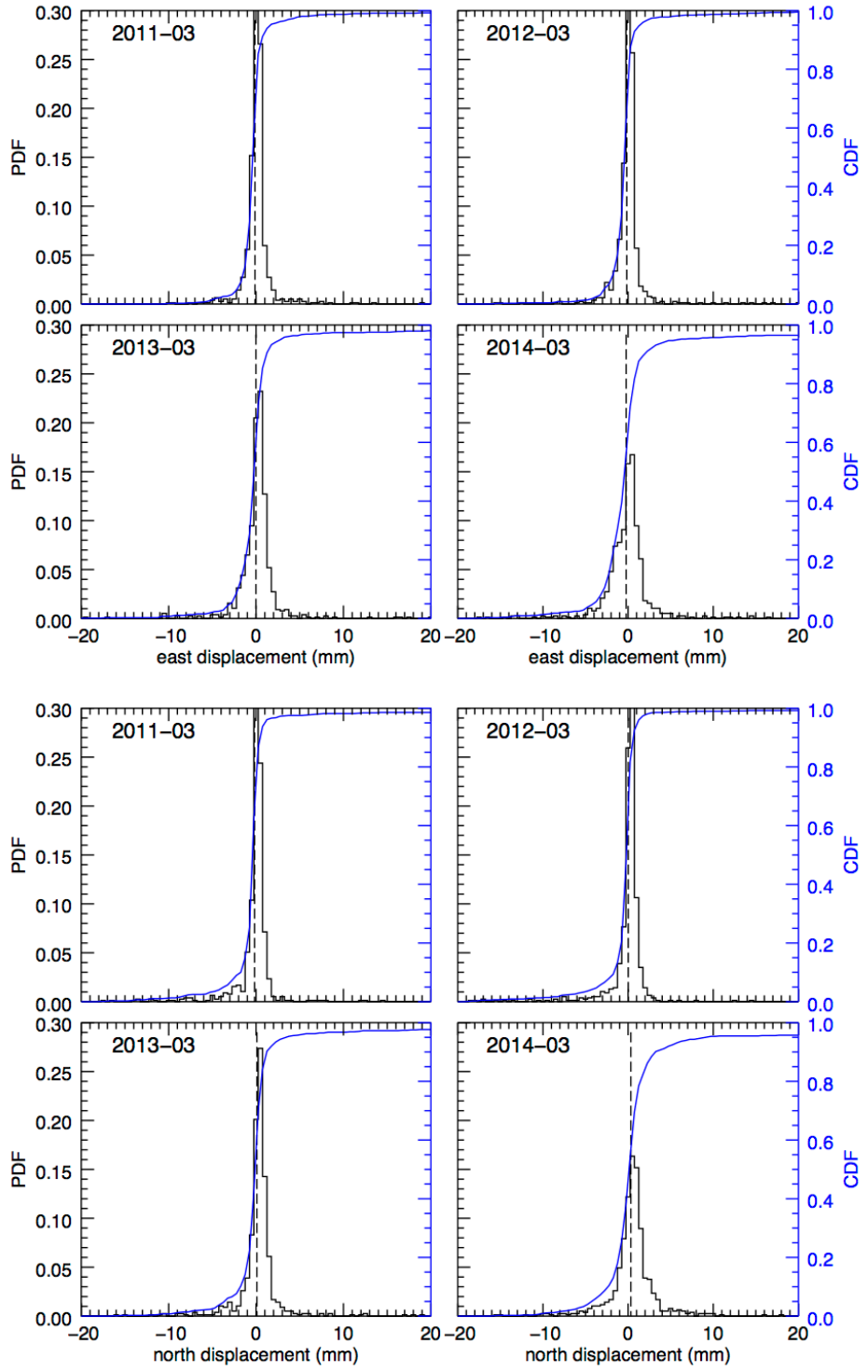

Fig. S4b

Histograms of East (top) and North (bottom) displacements shown in Fig. S3. In all cases, the spread of displacements is narrower than for the corresponding vertical displacements, and the median displacement is statistically indistinguishable from zero.

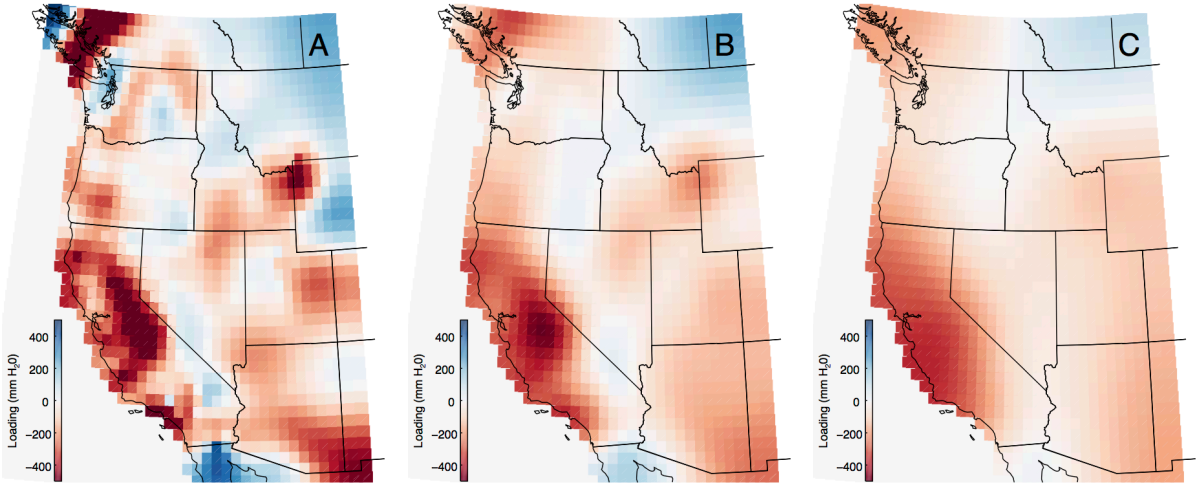

Fig. S5

Loading models with low (A), medium (B) and high (C) smoothing constraints applied during the inversion. The middle panel is the model shown in Fig. 3.

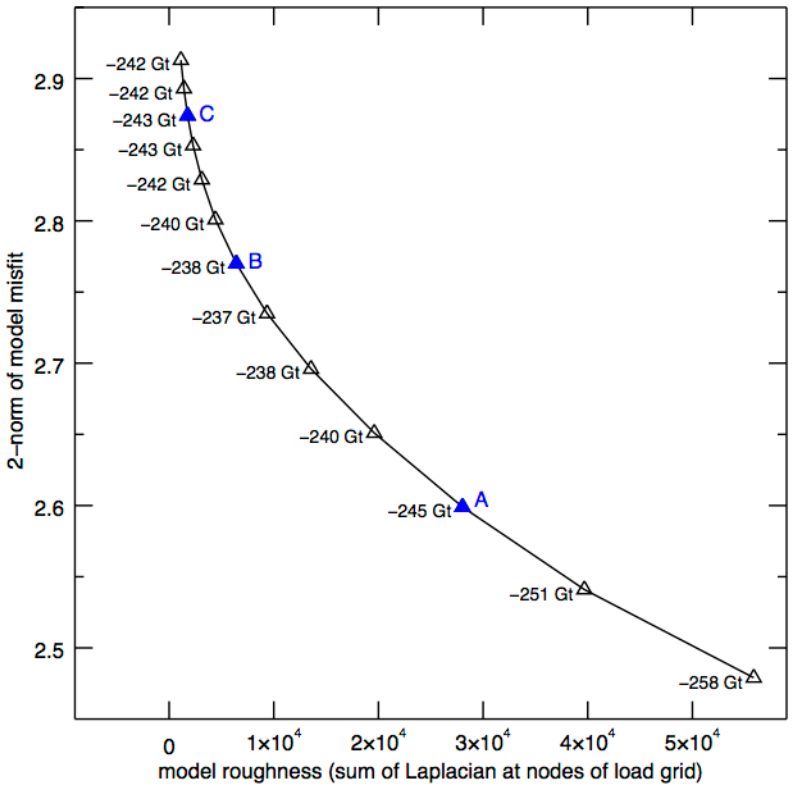

Fig. S6

Tradeoff between smoothness and misfit in loading inversion. Loading models in Fig. S5 are labeled with their corresponding letter, and total water deficit in gigatons over the WUSA is labeled for each model.

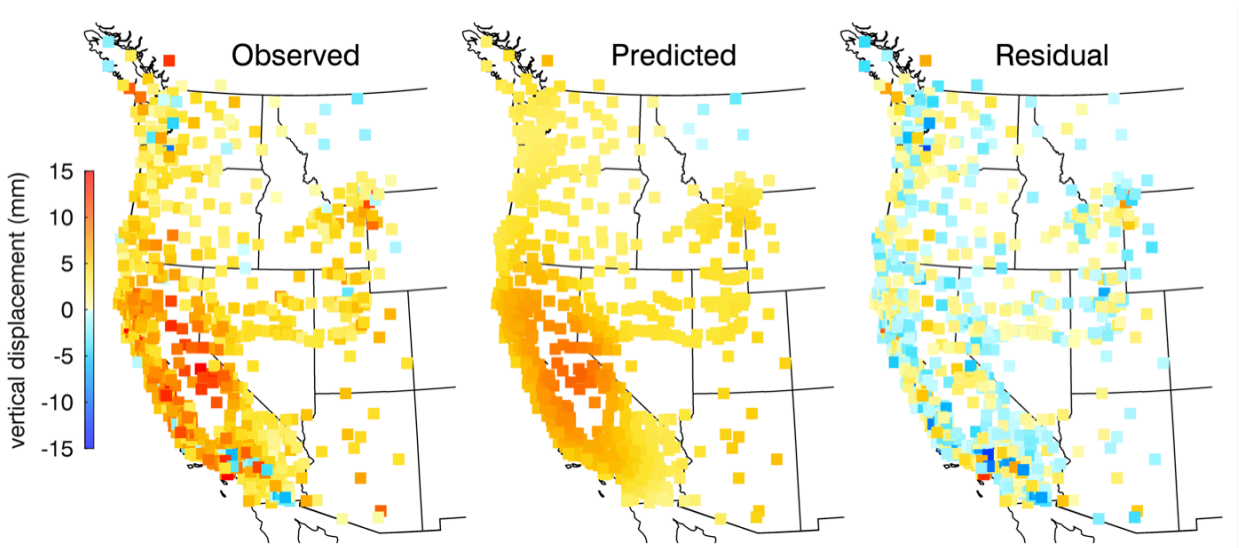

Fig. S7

Observed, predicted, and residual vertical displacements for the data shown in Fig. 2 (right panel) and the loading model in Fig. 3. Subtracting the predicted displacements from observed reduces the rms (root-mean-square) measure by 53%.

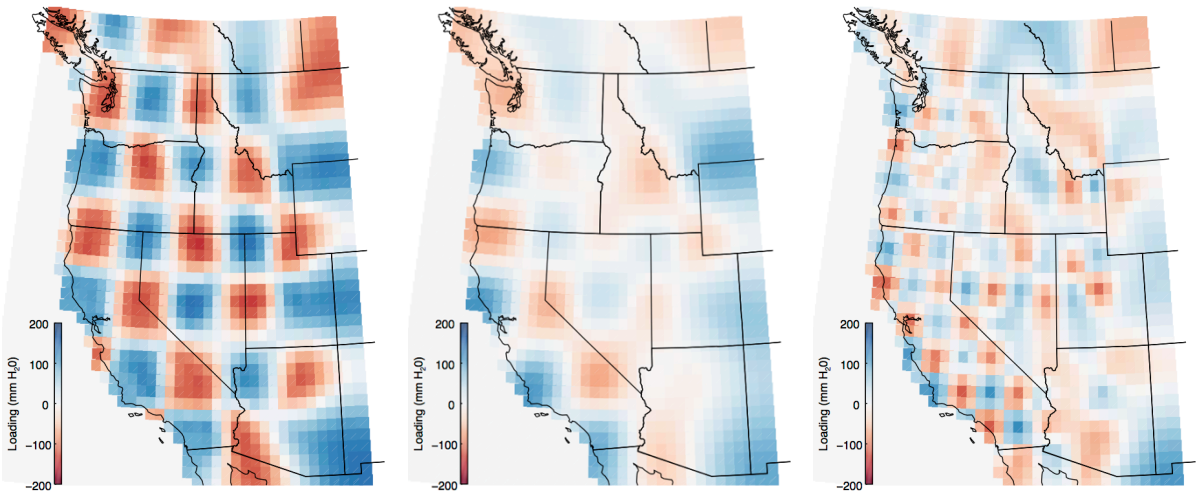

Fig. S8

Inversion tests using synthetic checkerboard patterns with positive and negative displacements juxtaposed. We used SPOTL to calculate vertical displacements at GPS station locations due to the checkerboard loading, then inverted these displacements to recover the original load. The left panel is the result from a loading model with a 3-degree grid, inverted with the smoothing parameter used in "A" in Fig. S5. The middle panel is the 3-degree model inverted with the smoothing used in "B" in Fig. S5, which gives in the same loading pattern, but with reduced peaks due to the higher smoothing. The right panel is a 1.5-degree model with the "A" smoothing, which shows that the current GPS network can easily resolve loading variations at wavelengths of 300 km in California, most of Nevada, and western Oregon and Washington.

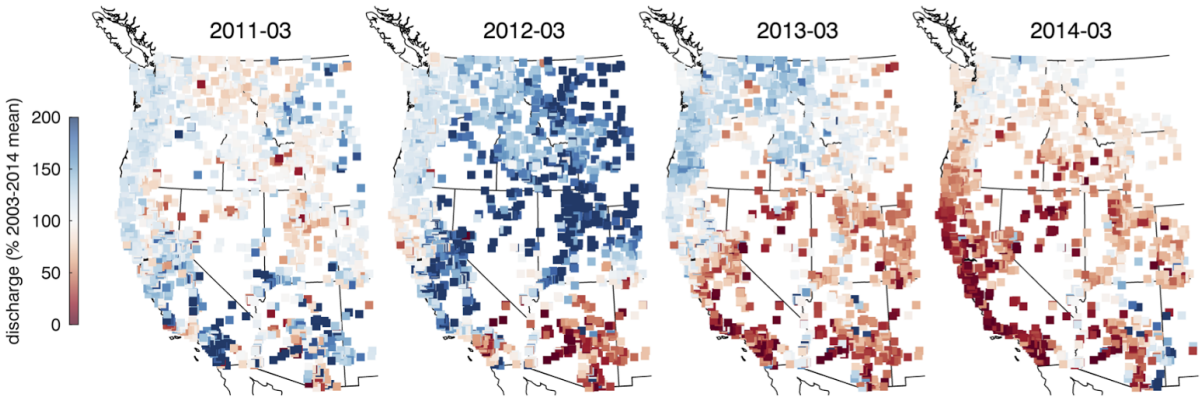

Fig. S9

Stream discharge % deviation from the 2003-2013 mean at 2950 stations in the USGS National Streamflow Information Program (NISP) network. These patterns are similar to that of the precipitation % deviation shown in Fig. 4.

References and Notes

1. F. Frappart, F. Papa, J. Santos da Silva, G. Ramillien, C. Prigent, F. Seyler, S. Calmant, Surface freshwater storage and dynamics in the Amazon basin during the 2005 exceptional drought. *Environ. Res. Lett.* **7**, 044010 (2012). doi:10.1088/1748-9326/7/4/044010

2. A. C. Thomas, J. T. Reager, J. S. Famiglietti, M. Rodell, A GRACE-based water storage deficit approach for hydrological drought characterization. *Geophys. Res. Lett.* **41**, 1537–1545 (2014). doi:10.1002/2014GL059323

3. W. E. Farrell, Deformation of the Earth by surface loads. *Rev. Geophys.* **10**, 761 (1972). doi:10.1029/RG010i003p00761

4. K. J. Ouellette, C. de Linage, J. S. Famiglietti, Estimating snow water equivalent from GPS vertical site-position observations in the western United States. *Water Resour. Res.* **49**, 2508–2518 (2013). Medline doi:10.1002/wrcr.20173

5. P. Elósegui, J. L. Davis, J. X. Mitrovica, R. A. Bennett, B. P. Wernicke, Crustal loading near Great Salt Lake, Utah. *Geophys. Res. Lett.* **30**, 1111 (2003). doi:10.1029/2002GL016579

6. J. Wahr *et al*., *J. Geophys. Res.* **117**, 9 (2013).

7. M. Bevis *et al*., Seasonal fluctuations in the mass of the Amazon River system and Earth's elastic response. *Geophys. Res. Lett.* **32**, L16308 (2005). doi:10.1029/2005GL023491

8. P. Bettinelli, J.-P. Avouac, M. Flouzat, L. Bollinger, G. Ramillien, S. Rajaure, S. Sapkota, Seasonal variations of seismicity and geodetic strain in the Himalaya induced by surface hydrology. *Earth Planet. Sci. Lett.* **266**, 332–344 (2008). doi:10.1016/j.epsl.2007.11.021

9. R. B. Cleveland, W. S. Cleveland, J. E. McRae, I. Terpenning, *J. Off. Stat.* **6**, 3 (1990).

10. M. S. Steckler, S. L. Nooner, S. H. Akhter, S. K. Chowdhury, S. Bettadpur, L. Seeber, M. G. Kogan, Modeling Earth deformation from monsoonal flooding in Bangladesh using hydrographic, GPS, and Gravity Recovery and Climate Experiment (GRACE) data. *J. Geophys. Res.* **115**, B08407 (2010). doi:10.1029/2009JB007018

11. D. Argus, Y. Fu, F. Landerer, Seasonal variation in total water storage in California inferred from GPS observations of vertical land motion. *Geophys. Res. Lett.* **41**, 1971–1980 (2014). doi:10.1002/2014GL059570

12. Materials and methods are available as supplementary materials on *Science* Online.

13. R. A. Bennett, Instantaneous deformation from continuous GPS: Contributions from quasi-periodic loads. *Geophys. J. Int.* **174**, 1052–1064 (2008). doi:10.1111/j.1365-246X.2008.03846.x

14. J. L. Davis, B. P. Wernicke, M. E. Tamisiea, On seasonal signals in geodetic time series. *J. Geophys. Res.* **117**, B01403 (2012). doi:10.1029/2011JB008690

15. D. Dzurisin, *Volcano Deformation: Geodetic Monitoring Techniques* (Springer, New York, 2007).

16. N. E. King *et al*., *J. Geophys. Res.* **112**, B03409 (2007).

17. D. L. Galloway, T. J. Burbey, Review: Regional land subsidence accompanying groundwater extraction. *Hydrogeol. J.* **19**, 1459–1486 (2011). doi:10.1007/s10040-011-0775-5

18. P. Elósegui, J. L. Davis, R. T. K. Jaldehag, J. M. Johansson, A. E. Niell, I. I. Shapiro, Geodesy using the Global Positioning System: The effects of signal scattering on estimates of site position. *J. Geophys. Res.* **100**, 9921 (1995). doi:10.1029/95JB00868

19. M. A. King, Z. Altamimi, J. Boehm, M. Bos, R. Dach, P. Elosegui, F. Fund, M. Hernández-Pajares, D. Lavallee, P. J. Mendes Cerveira, N. Penna, R. E. M. Riva, P. Steigenberger, T. Dam, L. Vittuari, S. Williams, P. Willis, Improved constraints on models of glacial isostatic adjustment: A review of the contribution of ground-based geodetic observations. *Surv. Geophys.* **31**, 465–507 (2010). doi:10.1007/s10712-010-9100-4

20. K.-H. Ji, T. A. Herring, A. L. Llenos, Near real-time monitoring of volcanic surface deformation from GPS measurements at Long Valley Caldera, California. *Geophys. Res. Lett.* **40**, 1054–1058 (2013). doi:10.1002/grl.50258

21. M. E. Ikehara, Global Positioning System surveying to monitor land subsidence in Sacramento Valley, California, USA. *Hydrol. Sci. J.* **39**, 417–429 (1994). doi:10.1080/02626669409492765

22. R. T. Hanson *et al*., in *Land Subsidence, Associated Hazards, and the Role of Natural Resources Development* (International Association of Hydrological Sciences, Wallingford, 2010), vol. 339, pp. 467–471.

23. R. Grapenthin, B. G. Ofeigsson, F. Sigmundsson, E. Sturkell, A. Hooper, Pressure sources versus surface loads: Analyzing volcano deformation signal composition with an application to Hekla volcano, Iceland. *Geophys. Res. Lett.* **37**, L20310 (2010). doi:10.1029/2010GL044590

24. D. C. Agnew, in *Treatise on Geophysics: Geodesy*, T. A. Herring, Ed. (Elsevier, New York, 2007), pp. 163–195.

25. D. C. Agnew, SPOTL: Some Programs for Ocean-Tide Loading, *SIO Technical Report*, Scripps Institution of Oceanography (2012); http://escholarship.org/uc/item/954322pg.

26. F. Pollitz, R. Bürgmann, W. Thatcher, Illumination of rheological mantle heterogeneity by the M7.2 2010 El Mayor-Cucapah earthquake. *Geochem. Geophys. Geosyst.* **13**, Q06002 (2012). doi:10.1029/2012GC004139

27. C. B. Amos, P. Audet, W. C. Hammond, R. Bürgmann, I. A. Johanson, G. Blewitt, Uplift and seismicity driven by groundwater depletion in central California. *Nature* **509**, 483–486 (2014). Medline doi:10.1038/nature13275

28. L. Astiz, P. M. Shearer, D. C. Agnew, Precise relocations and stress change calculations for the Upland earthquake sequence in southern California. *J. Geophys. Res.* **105**, 2937 (2000). doi:10.1029/1999JB900336

29. B. Smith-Konter, D. Sandwell, P. M. Shearer, Locking depths estimated from geodesy and seismology along the San Andreas fault system: Implications for seismic moment release. *J. Geophys. Res.* **116**, B06401 (2011). doi:10.1029/2010JB008117

30. M. Van Camp, O. de Viron, L. Métivier, B. Meurers, O. Francis, The quest for a consistent signal in ground and GRACE gravity time-series. *Geophys. J. Int.* **197**, 192–201 (2014). doi:10.1093/gji/ggt524

31. G. Ramillien, J. S. Famiglietti, J. Wahr, Detection of continental hydrology and glaciology signals from GRACE: A review. *Surv. Geophys.* **29**, 361–374 (2008). doi:10.1007/s10712-008-9048-9

32. K. M. Larson, J. J. Braun, E. E. Small, V. U. Zavorotny, E. D. Gutmann, A. L. Bilich, GPS multipath and its relation to near-surface soil moisture content. *IEEE J. Select. Top. Appl. Earth Obs. Remote Sens.* **3**, 91–99 (2010). doi:10.1109/JSTARS.2009.2033612

33. E. D. Gutmann, K. M. Larson, M. W. Williams, F. G. Nievinski, V. Zavorotny, Snow measurement by GPS interferometric reflectometry: An evaluation at Niwot Ridge, Colorado. *Hydrol. Processes* **26**, 2951–2961 (2012). doi:10.1002/hyp.8329

34. W. Wan, K. M. Larson, E. E. Small, C. C. Chew, J. J. Braun, Using geodetic GPS receivers to measure vegetation water content. *GPS Solut.* 10.1007/s10291-014-0383-7 (2014). doi:10.1007/s10291-014-0383-7

35. J. O. Langbein, F. Wyatt, H. Johnson, D. Hamann, P. Zimmer, Improved stability of a deeply anchored geodetic monument for deformation monitoring. *Geophys. Res. Lett.* **22**, 3533–3536 (1995). doi:10.1029/95GL03325